




Cite this: *Nanoscale Adv.*, 2019, 1, 4522

Synthesis of Au@TiO₂ core–shell nanoparticles with tunable structures for plasmon-enhanced photocatalysis†

Tian-Ming Chen,^a Ge-Yang Xu,^a He Ren,^a Hua Zhang,^a Zhong-Qun Tian ^a and Jian-Feng Li ^{*ab}

Plasmonic metal–semiconductor nanocomposites, especially those with core–shell nanostructures, have received extensive attention as they can efficiently expand light absorption and accelerate electron–hole separation thus improving the photocatalytic efficiency. However, controlled synthesis and structure manipulation of plasmonic metal–semiconductor nanocomposites still remain a significant challenge. Herein, a simple and universal method has been developed for the preparation of plasmonic Au@TiO₂ core–shell nanoparticles. Using such a method, uniform TiO₂ shells are successfully coated on Au nanoparticles with various morphologies including nanorods, nanocubes, and nanospheres, and the thickness and crystallinity of the TiO₂ shell can be simply tuned by adjusting the pH value and thermal treatment, respectively. Furthermore, the influence of the morphology of the Au core and the thickness and crystallinity of the TiO₂ shell on the photocatalytic performance of Au@TiO₂ towards the photodegradation of methylene blue is systematically explored. It is found that Au@TiO₂ NPs with nanorod morphology and crystalline TiO₂ shells display the best performance, which is 5 times higher than that of bare Au nanoparticles. This work provides a facile strategy for the fabrication of plasmonic core–shell nanostructures that show excellent performance in plasmon-enhanced photocatalysis.

Received 31st August 2019
Accepted 9th October 2019

DOI: 10.1039/c9na00548j

rsc.li/nanoscale-advances

Introduction

With the depletion of fossil fuels and increasing serious environmental pollution, research on photocatalysis using solar energy has intensified.^{1–5} TiO₂ has emerged as a good photocatalyst candidate owing to its abundance in nature, low cost, non-toxicity, and photochemical stability. However, TiO₂ has a wide bandgap of 3.2 eV, thus its photoresponse is limited to the ultraviolet region, significantly hindering its solar energy conversion efficiency.^{6–9}

In the past few decades, various strategies have been proposed to improve the photocatalytic activity of TiO₂, such as doping with metal/non-metal elements or ions,^{10–13} organic dye sensitization,^{14,15} and forming nanocomposites with other semiconductors.^{16,17} However, most of these proposed solutions only slightly extend the photoresponse of TiO₂ to the visible region, and the absorption coefficient still remains small.

Plasmonic nanostructures, such as Au, Ag, and Cu, have extremely large absorption/scattering cross sections in the visible light region due to the surface plasmon resonance (SPR) effect,^{18–27} and have been applied in many fields, especially in plasmon-enhanced spectroscopy (PES).^{28–30} The SPR effect enables the injection of hot electrons generated on these noble metals into nearby semiconductors thus expanding the light absorption range of the semiconductor.^{20,22,31} Besides the hot electron injection mechanism, the SPR effect also benefits photocatalysis by generating strong electromagnetic fields in the near field of metal nanoparticles (NPs) to accelerate electron–hole separation and increasing light scattering for the reuse of unabsorbed light.^{18,19,27} These advantages make plasmon-enhanced photocatalysis a research hotspot.

However, these mechanisms for boosting photocatalytic activity rely on the synthesis and manipulation of metal–semiconductor composites. Therefore, rational design and construction of metal–semiconductor nanostructures are particularly important. A common nanostructure is constructed by loading noble metal nanoparticles (NPs) onto semiconductor surfaces, such as Au–TiO₂,^{32,33} Au–CdS,^{34,35} Au–ZnO,^{36,37} Au–Fe₂O₃,³⁸ etc. In this case, the photocatalytic efficiency can be improved to a certain level. However, it is difficult to fully utilize the SPR properties of the metal NPs due to the very limited interaction between the metal and the semiconductor in such

^aMOE Key Laboratory of Spectrochemical Analysis and Instrumentation, State Key Laboratory of Physical Chemistry of Solid Surfaces, iChem, College of Chemistry and Chemical Engineering, College of Materials, College of Energy, Xiamen University, Xiamen 361005, China. E-mail: Li@xmu.edu.cn

^bShenzhen Research Institute of Xiamen University, Shenzhen 518000, China

† Electronic supplementary information (ESI) available: Fig. S1 and S2. See DOI: 10.1039/c9na00548j



Herein, we report a simple and universal method to synthesize Au@TiO₂ core-shell nanostructures. Au cores with three morphologies including nanocubes, nanorods, and nanospheres are successfully synthesized, and the shell thickness is well controlled with the choice of the Ti precursor and adjustment of the pH value. Additionally, annealing treatment could transform the amorphous TiO₂ shell into a crystalline one. Finally, the photocatalytic performance of the Au@TiO₂ core-shell nanoparticles towards the degradation of methylene blue is investigated. The results show that the photocatalytic activity is mainly dependent on the SPR effect and that the crystalline shell can greatly improve the catalytic activity. This strategy provides a platform for constructing plasmonic core-shell photocatalysts with improved performance.

Materials

Chloroauric acid tetrahydrate ($\text{HAuCl}_4 \cdot 4\text{H}_2\text{O}$, AR), hexadecyl trimethyl ammonium chloride (CTAC, >99%), hexadecyl trimethyl ammonium bromide (CTAB, >99%), sodium dodecyl sulfate (SDS), NaHCO_3 (>99%), NaBH_4 (98%), ascorbic acid (AA, AR), AgNO_3 (>99%), and HCl (30%) were purchased from Sinopharm Reagents Co. (China). Titanium trichloride (TiCl_3 , 15–20%) was purchased from Sigma Aldrich. Ultra-pure Milli-Q water (18.2 M Ω cm) was used throughout the study.

The Au nanospheres were synthesized using the seed-mediated method.⁵¹ First, 0.25 mL of HAuCl₄ solution (0.01 M) was added

To synthesize Au nanospheres (NSs), 30 mL of CTAC solution (0.025 M), 0.75 mL of AA solution (0.1 M), 1.5 mL of HAuCl₄ solution (0.01 M) and 1.5 mL of seed 2 solution were then mixed uniformly and placed in a 45 °C water bath for 3 hours. This solution was then centrifuged and redispersed in 30 mL of CTAB solution (0.02 M) and 1.5 mL of HAuCl₄ solution (0.01 M), and then allowed to react by putting in a 45 °C water bath for 2 hours to obtain the Au NSs.

Ligand exchange of Au nanostructures was first performed using SDS in the following steps: typically, a solution (10 mL) of an as-prepared metal nanocrystal sample that was stabilized with either CTAB or CTAC was washed once by centrifugation to remove the excess surfactant and then redispersed in water (10 mL). The resultant metal nanocrystal solution was added dropwise under vigorous stirring to an aqueous SDS solution (10 mL, 0.1 M). SDS adsorption was allowed for at least 0.5 h at room temperature. After the excess SDS was removed by centrifugation, the SDS-encapsulated metal nanocrystals were redispersed in water (50 μ L). It should be noted that the concentration of SDS remaining in the nanocrystal solution should be as low as possible to avoid the self-growth of TiO_2 . In a typical synthesis, 50 μ L of TiCl_3 solution was mixed with 6 mL of Milli-Q water, and 0.1 M NaHCO_3 solution was added under stirring. Then, the concentrated Au-SDS solution was quickly mixed with the TiCl_3 - NaHCO_3 solution, stirred for 10 min, and

washed twice with ethanol to obtain Au@TiO₂ core-shell nanostructures.

Synthesis of crystallized Au@TiO₂ core-shell NPs

The as-prepared Au@TiO₂ core-shell nanostructure sample was washed and transferred into a quartz crucible with absolute alcohol (1 mL). Then the quartz crucible was placed in a muffle furnace and annealed at 300 °C or 500 °C for 2 hours. Finally, the calcined core-shell nanostructure sample was redispersed in water (2 mL) by ultrasonication.

Photocatalytic measurements

A 150 W Xe lamp with a 420 nm filter channel was used as the light source. 5 mg of TiO₂ or Au@TiO₂ photocatalyst were dispersed in 30 mL of MB (5 ppm) aqueous solution. The solution was continuously stirred in the dark for about 1 hour to establish an adsorption-desorption equilibrium between the photocatalyst and the dye. The suspension was then irradiated with the 150 W Xe lamp or with light having a wavelength longer than 420 nm. During the irradiation, the solution was stirred to maintain the suspension. After 2 hours, an aliquot of the suspension was taken and centrifuged. The residual concentration of MB was monitored using a UV-vis spectrophotometer.

Characterization

The morphology of the Au@TiO₂ NPs was characterized by transmission electron microscopy (TEM, JEOL JEM 1400; HR-TEM, JEOL JEM 2100). EDS mapping analysis was performed on a field emission transmission electron microscope (TEM, Philips TECNAI F30). Absorption spectra were collected on an ultraviolet-visible spectrophotometer (UNICO, UV2012C/PC/PCS). X-ray diffraction (XRD) studies were carried out on an X-ray diffractometer (Rigaku IV) using Cu K radiation ($\lambda = 1.5418 \text{ \AA}$). A confocal Raman spectrometer (HORIBA, X-plora) was used to record Raman signals.

Results and discussion

Fig. 1 illustrates the formation process of TiO₂ shell-coated Au NPs, using Au NR@TiO₂ core-shell nanostructures as an example. First, Au NRs are prepared by the seed growth method, and the NRs are stabilized with cetyltrimethylammonium bromide (CTAB) and positively charged. Next, the negative charge modifier, SDS, is added to modify the surface of Au NRs by electrostatic attractions. TiCl₃ is chosen as the titanium dioxide precursor because of its relatively low hydrolysis rate. By

controlling the pH value, TiCl₃ is then hydrolyzed to TiOH²⁺ and adsorbed by the negatively charged SDS layer. Finally, the dissolved oxygen in the solution oxidized the Ti³⁺ species to the TiO₂ shell at room temperature.⁴⁹

The as-prepared core-shell NPs are characterized by TEM (Fig. 2a–l). To demonstrate the universal applicability of this method, we have prepared three different nanostructure Au cores: Au NRs (length: $120 \pm 10 \text{ nm}$; diameter: $60 \pm 5 \text{ nm}$), Au NCs (diameter: $50 \pm 5 \text{ nm}$) and Au NSs (diameter: $65 \pm 5 \text{ nm}$). It can be seen from the TEM images that the as-prepared core-shell NPs show uniform morphologies and good dispersion. By controlling the pH below 2.5, the TiO₂ shell is formed by close aggregation of many small amorphous TiO₂ NPs, and no self-nucleation of TiO₂ is found. Different TiO₂ shell thicknesses are obtained by controlling the reaction time and pH of the solution. As shown in Fig. 2, the thickness of the TiO₂ shells of the three kinds of Au@TiO₂ nanostructures can be controlled between 4 and 30 nm. The shell layer only grows along the surface of the core, keeping the shell morphology the same as that of the core.

The structure and composition of Au NR@TiO₂ were further investigated by high angle annular dark field scanning transmission electron microscopy (HAADF-STEM) and elemental mapping analysis (Fig. 2m–p). These results show that the core is composed of Au, while the shell layer is composed of Ti and O, confirming the formation of the Au@TiO₂ core-shell nanostructures. It is well known that the SPR of Au NPs is highly sensitive to the size, shape, structure, and surrounding dielectric environment.^{27,52} To study how the TiO₂ shell affects the SPR of Au NPs, we have examined the UV-vis absorption spectra of bare Au and the corresponding Au@TiO₂ nanostructures. Fig. 2q displays the change in the LSPR band of three kinds of Au@TiO₂ nanostructures. For the nanorod-core nanostructures, the transverse plasmon peak red-shifts from 514 nm to 527 nm and the longitudinal plasmon peak red-shifts from 672 nm to 721 nm. For the nanocube-core one, the plasmon peak red-shifts from 540 nm to 566 nm. For the nanosphere-core, the plasmon peak red-shifts from 535 nm to 561 nm. And the UV-vis absorption spectra of Au NRs@TiO₂ NPs with different TiO₂ shell thickness are measured as shown in Fig. S1.† It can be seen that a red shift is observed when the TiO₂ shell becomes thicker. The red-shift of the plasmon band in the UV-vis absorption spectra after TiO₂ coating is caused by the increase of the refractive index of the surrounding medium.⁴⁹

We find that the structure and crystallinity of Au@TiO₂ nanoparticles are largely affected by the thermal treatment temperature. As shown in Fig. 3a, before thermal treatment, the TiO₂ shell shows an amorphous and porous structure. Whereas in Fig. 3b, after annealing at 300 °C, the shell is visibly thinner and formed of small TiO₂ grains. This indicates that the shell changes while the size and shape of the Au core remain stable. Increasing the temperature to 500 °C makes the shell denser and smoother than at 300 °C. However, the Au core also deforms (Fig. 3c). HR-TEM imaging clearly shows changes in the TiO₂ lattice due to crystallization (Fig. 3d–f). No obvious lattice fringes are found before annealing; however, after 300 °C treatment, lattice fringes appeared, with a lattice spacing of

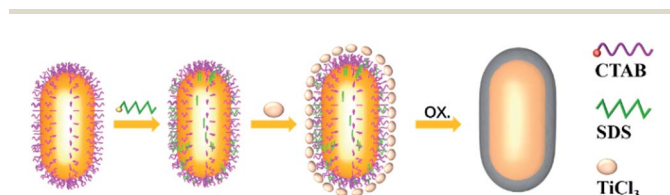


Fig. 1 Schematic diagram of the preparation of Au NR@TiO₂ nanostructures by coating TiO₂ on Au NRs.





Fig. 2 (a) TEM image of Au NRs (length: 120 ± 10 nm; diameter: 60 ± 5 nm), (b–d) TEM images of Au NR@TiO₂ with different coating thicknesses (shell thickness: 4 ± 1 nm, 15 ± 2 nm, and 30 ± 4 nm). (e) TEM images of Au NCs (diameter: 50 ± 5 nm), (f–h) TEM images of Au NC@TiO₂ with different coating thicknesses (shell thickness: 4 ± 1 nm, 10 ± 2 nm, and 20 ± 4 nm). (i) TEM images of Au NSs (diameter: 65 ± 5 nm). (j–l) TEM images of Au NS@TiO₂ with different coating thicknesses (shell thickness: 5 ± 1 nm, 15 ± 2 nm, and 30 ± 4 nm). (m) HAADF-STEM image of a single Au NR@TiO₂ nanostructure. (n–p) Elemental distribution map of Au, Ti and O. (q) UV-visible absorption spectra of uncoated Au NRs, Au NCs, Au NSs (dashed lines), Au NR@TiO₂ (shell thickness: 15 nm), Au NC@TiO₂ (shell thickness: 10 nm), and Au NS@TiO₂ (shell thickness: 15 nm) core-shell nanostructures (solid-lines).

0.35 nm, corresponding to the (200) plane of anatase (Fig. 3e). After annealing at 500 °C, the lattice fringes are clearer, while the lattice spacing is unchanged at 0.35 nm (Fig. 3f).

The XRD pattern provides further evidence for the formation of TiO₂ shell crystals (Fig. 3g). Before the thermal treatment, only the typical Au (111) and Au (220) diffraction peaks (JCPDS card no. 65-8601) can be seen, indicating that the TiO₂ shell is amorphous. However, after annealing at 300 °C, diffraction peaks at 25.3°, 48.1°, 54.0°, 55.1°, and 62.8° appear, which can be assigned to anatase TiO₂ (JCPDS card no. 01-0562). After annealing at 500 °C, the characteristic peak of TiO₂ shows higher intensities and clearer contours, indicating a more crystalline structure, consistent with TEM observations. These results verify that the structure of Au@TiO₂ and the TiO₂ shell (amorphous and crystalline) can be tuned through thermal treatment.

Fig. 3h displays the UV-vis spectra of Au NR@TiO₂ nanostructures before and after crystallization. After thermal treatment at 300 °C, the longitudinal plasmon peak red-shifts from 721 nm to 770 nm. As the thermal temperature rises to 500 °C, the longitudinal plasmon peak continues to red-shift to 796 nm. Besides, we can clearly find that the Au NR@TiO₂ sample after thermal treatment shows a significant increase in absorbance at around 400 nm, which is caused by crystalline TiO₂. The possible causes of the red-shift of the plasmon peak are summarized through these experimental phenomena. First, the thermal treatment of the Au@TiO₂ nanostructure results in a phase transition of the TiO₂ shell from the amorphous phase to the anatase phase. The increase in the crystallinity of TiO₂ leads to an increase in the dielectric constant, resulting in a redshift of the SPR absorption band. Second, it has been

reported early that when the contact area of Au and TiO₂ increases, the peak of the SPR band shifts to a longer wavelength.³² As shown in the TEM image, the heat treatment increases the contact area between Au and TiO₂, thus causing a redshift in the SPR band.

Furthermore, Fig. 3i shows the Raman spectra of the sample before and after annealing. It can be found that after annealing, the peak shape at 690 cm⁻¹ for TiO₂ becomes sharper and red-shifts, indicating that annealing changes its crystallinity. The Raman signals for carbon deposition between 1200 cm⁻¹ and 1600 cm⁻¹ resulting from the CTAB impurity disappear, indicating that annealing removes impurities of the core-shell structure. These results confirm that the crystallization and porous state of the shell layer in the Au@TiO₂ core-shell structure can be adjusted by thermal treatment.

The influence of the Au core morphology and the shell crystallinity and thickness on the photocatalytic activity of different Au@TiO₂ core-shell NPs is evaluated using the photocatalytic degradation of methylene blue, a common environmental pollutant. Fig. 4a and S2† show the photocatalytic performance of Au NR@TiO₂ core-shell nanostructures treated at different temperatures. Blank experiments show that self-degradation of methylene blue is minimal. Au NRs or TiO₂ before and after annealing treatment also shows very weak catalytic activity under visible light illumination. The Au@TiO₂ activity without thermal treatment is slightly better than that of TiO₂, indicating that the SPR effect of Au has a positive effect on the photocatalytic activity of TiO₂. However, the activity of Au@TiO₂ is significantly enhanced after annealing. The degradation efficiencies of Au@TiO₂-300 and Au@TiO₂-500 in 2 h are 33% and 26%, respectively, which are 5





Fig. 3 (a and d) TEM images and HR-TEM images before annealing and at (b and e) 300 °C and (c and f) 500 °C. (g) XRD of Au@TiO₂ nanostructures before and after annealing. (h) UV-visible spectroscopy of Au@TiO₂ nanostructures before and after annealing. (i) Raman spectroscopy of Au@TiO₂ nanostructures before and after annealing.

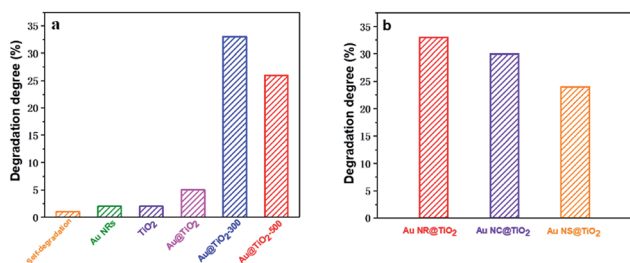


Fig. 4 (a) Photocatalytic degradation of methylene blue by Au NRs, TiO₂ and annealed Au@TiO₂ core-shell nanostructures under visible light. (b) Photocatalytic degradation of methylene blue by Au NR@TiO₂, Au NC@TiO₂ and Au NS@TiO₂ core-shell nanostructures after annealing under visible light.

times and 4 times higher than that of the unannealed sample. The annealing process facilitates the transportation of hot electrons to the crystalline shell. Additionally, it eliminates impurities in the materials so that there are better contact and stronger interactions between the Au core and TiO₂ shell.

Further increasing the temperature to 500 °C decreases the catalytic activity, probably due to the loss of active sites and the destruction of the porous shell at high temperature. The Au core also shows some deformation at 500 °C, which can weaken its SPR performance.

The effects of Au-core morphology on the photocatalytic activities are also investigated. In this case, all the samples are calcined at 300 °C, and the quantity of the catalyst and thickness of the TiO₂ shell are kept the same. As shown in Fig. 4b, nanorods have superior activity over the other two types of NPs. This is likely due to nanorods having two plasmonic modes, *i.e.* transverse and longitudinal modes, which both contribute to light capturing.⁵

To better understand how the SPR effect affects the photocatalytic activity, first, each core-shell nanostructure is annealed at 300 °C, and the photocatalytic degradation of methylene blue using Au NR@TiO₂ NPs with the same amount of Au cores and different shell thicknesses under full and visible light illumination is studied (Fig. 5a). Under visible light illumination, the 5 nm shell shows the highest activity, achieving





Fig. 5 (a) Photocatalytic degradation of methylene blue by Au NR@TiO₂ core-shell nanostructures with different shell thicknesses under full light and visible light illumination. (b) Mechanistic diagram of Au NR@TiO₂ core-shell nanostructure enhanced photocatalysis under illumination.

a photodegradation efficiency of 46%. As the shell thickness increases, the catalytic activity decreases rapidly corresponding to the decreased SPR intensity and a reduction of hot electron injection rates, with the photodegradation efficiency of the 20 nm shell NPs being only 12%. Under full light illumination, the photodegradation efficiency also decreases as the shell thickness increases. However, the rate of decrease is more moderate than that with visible light. The photodegradation efficiency of samples with 5 nm and 20 nm shells is 65% and 47%, respectively. Furthermore, bare Au NRs show much lower activity compared to the Au NR@TiO₂ NPs. These results illustrate that the SPR effect is the dominant factor causing the higher photocatalytic activity.

Based on the analysis of experimental results, the mechanism of Au@TiO₂ core-shell nanostructure enhanced photocatalysis is summarized in Fig. 5b. Au NRs standards alone also show very weak catalytic activity under full light or visible light. Under visible light, although TiO₂ is inactive, Au NPs can generate hot carriers which can induce photocatalysis. Obviously, the thicker the shell, the harder it is for hot carriers to reach the TiO₂ surface and the lower the catalytic activity.²¹ Under full light illumination, photoelectrons can be generated in TiO₂ and participate in the photocatalytic reaction. In this case, nanoparticles have better catalytic activities when they have thicker shells, *i.e.*, a larger amount of TiO₂. At the same time, hot carriers and an electromagnetic field are also generated by the Au nanoparticles under such a condition, which would benefit the reaction. However, such an influence would decrease with the increase of shell thickness. As a result, a balance is achieved when the photocatalytic performance under full light illumination shows a moderate decrease as the shell thickness increases. According to previous studies, the electron transfer from Au to TiO₂ plays a primary role in enhancing the photocatalytic activity under full light.²² Therefore, the change of photocatalytic activity is consistent with the trend of the decreased SPR intensity under full light and visible light illumination, indicating that the SPR effect is the main factor to improve the photocatalytic performance.

Conclusions

In summary, a simple, repeatable, and universal method for coating TiO₂ onto different Au core nanostructures has been developed. After shell coating, the morphology of the Au core is preserved and the structure of the photocatalysts is well controlled with good dispersibility. The effects of the crystallinity and thickness of the TiO₂ shell and the Au core morphology on the photocatalytic activity of the catalysts are also studied in detail. Owing to better transportation of hot electrons, annealing the amorphous shell to form a crystalline TiO₂ shell considerably improved the photocatalytic activity of the NPs. Among the different morphologies screened, Au NR core photocatalysts showed the highest activity due to better light absorption. Finally, by comparing photocatalysts with different shell thicknesses, we propose that hot electron transfer from the Au core is the main factor dictating the photocatalytic activity, regardless of whether under full light or visible light illumination. We believe that the plasmonic core-semiconductor shell nanocomposite can play an important role in photocatalysis by manipulating the structure and composition in the future.

Conflicts of interest

There are no conflicts to declare.

Acknowledgements

This work was supported by the NSFC (21775217, 21703181, 21427813, and 21521004), the Fundamental Research Funds for the Central Universities (20720190044), the Natural Science Foundation of Guangdong Province (2016A030308012), the Basic Research Projects of Shenzhen Research & Development Fund (JCYJ20170306140934218), and the Open Fund of the State Key Laboratory of Luminescent Materials and Devices (South China University of Technology).

Notes and references

- 1 C. C. Chen, W. H. Ma and J. C. Zhao, *Chem. Soc. Rev.*, 2010, **39**, 4206–4219.
- 2 X. X. Chang, T. Wang and J. L. Gong, *Energy Environ. Sci.*, 2016, **9**, 2177–2196.
- 3 Y. Ma, X. L. Wang, Y. S. Jia, X. B. Chen, H. X. Han and C. Li, *Chem. Rev.*, 2014, **114**, 9987–10043.
- 4 S. C. Warren and E. Thimsen, *Energy Environ. Sci.*, 2012, **5**, 5133–5146.
- 5 W. B. Hou and S. B. Cronin, *Adv. Funct. Mater.*, 2013, **23**, 1612–1619.
- 6 D. J. Yang, H. W. Liu, Z. F. Zheng, Y. Yuan, J. C. Zhao, E. R. Waclawik, X. B. Ke and H. Y. Zhu, *J. Am. Chem. Soc.*, 2009, **131**, 17885–17893.
- 7 X. B. Chen, L. Liu and F. Q. Huang, *Chem. Soc. Rev.*, 2015, **44**, 1861–1885.
- 8 Q. J. Xiang, J. G. Yu and M. Jaroniec, *J. Am. Chem. Soc.*, 2012, **134**, 6575–6578.



- 9 W. E. Kaden, T. P. Wu, W. A. Kunkel and S. L. Anderson, *Science*, 2009, **326**, 826–829.
- 10 B. A. Rosen, A. Salehi-Khojin, M. R. Thorson, W. Zhu, D. T. Whipple, P. J. A. Kenis and R. I. Masel, *Science*, 2011, **334**, 643–644.
- 11 R. Asahi, T. Morikawa, T. Ohwaki, K. Aoki and Y. Taga, *Science*, 2001, **293**, 269–271.
- 12 A. P. Bhirud, S. D. Sathaye, R. P. Waichal, J. D. Ambekar, C. J. Park and B. B. Kale, *Nanoscale*, 2015, **7**, 5023–5034.
- 13 G. S. Zhang, Y. C. Zhang, M. Nadagouda, C. Han, K. O'Shea, S. M. El-Sheikh, A. A. Ismail and D. D. Dionysiou, *Appl. Catal., B*, 2014, **144**, 614–621.
- 14 A. Yella, H. W. Lee, H. N. Tsao, C. Y. Yi, A. K. Chandiran, M. K. Nazeeruddin, E. W. G. Diau, C. Y. Yeh, S. M. Zakeeruddin and M. Gratzel, *Science*, 2011, **334**, 629–634.
- 15 G. S. Li, B. Jiang, S. N. Xiao, Z. C. Lian, D. Q. Zhang, J. C. Yu and H. X. Li, *Environ. Sci.: Processes Impacts*, 2014, **16**, 1975–1980.
- 16 C. Eley, T. Li, F. L. Liao, S. M. Fairclough, J. M. Smith, G. Smith and S. C. E. Tsang, *Angew. Chem., Int. Ed.*, 2014, **53**, 7838–7842.
- 17 H. Tada, T. Mitsui, T. Kiyonaga, T. Akita and K. Tanaka, *Nat. Mater.*, 2006, **5**, 782–786.
- 18 V. Giannini, A. I. Fernandez-Dominguez, S. C. Heck and S. A. Maier, *Chem. Rev.*, 2011, **111**, 3888–3912.
- 19 S. Linic, P. Christopher and D. B. Ingram, *Nat. Mater.*, 2011, **10**, 911–921.
- 20 C. Boerigter, R. Campana, M. Morabito and S. Linic, *Nat. Commun.*, 2016, **7**, 10545.
- 21 M. L. Brongersma, N. J. Halas and P. Nordlander, *Nat. Nanotechnol.*, 2015, **10**, 25–34.
- 22 K. Wu, J. Chen, J. R. McBride and T. Lian, *Science*, 2015, **349**, 632–635.
- 23 A. Sanchez-Iglesias, A. Chuvilin and M. Grzelczak, *Chem. Commun.*, 2015, **51**, 5330–5333.
- 24 N. Zhou, V. Lopez-Puente, Q. Wang, L. Polavarapu, I. Pastoriza-Santos and Q. H. Xu, *RSC Adv.*, 2015, **5**, 29076–29097.
- 25 J.-F. Li, Y.-J. Zhang, S.-Y. Ding, R. Panneerselvam and Z.-Q. Tian, *Chem. Rev.*, 2017, **117**, 5002–5069.
- 26 C. G. Silva, R. Juarez, T. Marino, R. Molinari and H. Garcia, *J. Am. Chem. Soc.*, 2011, **133**, 595–602.
- 27 S. Mubeen, J. Lee, N. Singh, S. Kramer, G. D. Stucky and M. Moskovits, *Nat. Nanotechnol.*, 2013, **8**, 247–251.
- 28 J. F. Li, Y. F. Huang, Z. L. Yang, D. Y. Wu, B. Ren, Z. L. Wang and Z. Q. Tian, *Nature*, 2010, **464**, 392–395.
- 29 C.-Y. Li, J.-B. Le, Z.-L. Yang, J.-F. Li, J. Cheng and Z.-Q. Tian, *Nat. Mater.*, 2019, **18**, 697–701.
- 30 J.-C. Dong, X.-G. Zhang, V. Briega-Martos, X. Jin, S. Chen, Z.-L. Yang, D.-Y. Wu, J. M. Feliu, C. T. Williams, Z.-Q. Tian and J.-F. Li, *Nat. Energy*, 2019, **4**, 60–67.
- 31 M. J. Kale, T. Avanesian and P. Christopher, *ACS Catal.*, 2014, **4**, 116–128.
- 32 M. Murdoch, G. I. N. Waterhouse, M. A. Nadeem, J. B. Metson, M. A. Keane, R. F. Howe, J. Llorca and H. Idriss, *Nat. Chem.*, 2011, **3**, 489–492.
- 33 A. Luken, M. Muhler and J. Strunk, *Phys. Chem. Chem. Phys.*, 2015, **17**, 10391–10397.
- 34 J. Xu, W. M. Yang, S. J. Huang, H. Yin, H. Zhang, P. Radjenovic, Z. L. Yang, Z. Q. Tian and J. F. Li, *Nano Energy*, 2018, **49**, 363–371.
- 35 K. F. Wu, W. E. Rodriguez-Cordoba, Y. Yang and T. Q. Lian, *Nano Lett.*, 2013, **13**, 5255–5263.
- 36 J. Strunk, K. Kaehler, X. Y. Xia, M. Comotti, F. Schuth, T. Reinecke and M. Muhler, *Appl. Catal., A*, 2009, **359**, 121–128.
- 37 P. Li, Z. Wei, T. Wu, Q. Peng and Y. D. Li, *J. Am. Chem. Soc.*, 2011, **133**, 5660–5663.
- 38 H. Yu, M. Chen, P. M. Rice, S. X. Wang, R. L. White and S. H. Sun, *Nano Lett.*, 2005, **5**, 379–382.
- 39 B. X. Li, T. Gu, T. Ming, J. X. Wang, P. Wang, J. F. Wang and J. C. Yu, *ACS Nano*, 2014, **8**, 8152–8162.
- 40 K. S. Mayya, D. I. Gittins and F. Caruso, *Chem. Mater.*, 2001, **13**, 3833–3836.
- 41 D. Y. Liu, S. Y. Ding, H. X. Lin, B. J. Liu, Z. Z. Ye, F. R. Fan, B. Ren and Z. Q. Tian, *J. Phys. Chem. C*, 2012, **116**, 4477–4483.
- 42 T. Hirakawa and P. V. Kamat, *J. Am. Chem. Soc.*, 2005, **127**, 3928–3934.
- 43 F. Bao, J. L. Yao and R. A. Gu, *Langmuir*, 2009, **25**, 10782–10787.
- 44 X. N. Fu, J. Liu, H. Yang, J. C. Sun, X. Li, X. K. Zhang and Y. X. Jia, *Mater. Chem. Phys.*, 2011, **130**, 334–339.
- 45 I. Lee, J. B. Joo, Y. D. Yin and F. Zaera, *Angew. Chem., Int. Ed.*, 2011, **50**, 10208–10211.
- 46 N. Zhou, L. Polavarapu, N. Y. Gao, Y. L. Pan, P. Y. Yuan, Q. Wang and Q. H. Xu, *Nanoscale*, 2013, **5**, 4236–4241.
- 47 W. L. Liu, F. C. Lin, Y. C. Yang, C. H. Huang, S. Gwo, M. H. Huang and J. S. Huang, *Nanoscale*, 2013, **5**, 7953–7962.
- 48 X. Li, X. N. Fu and H. Yang, *Phys. Chem. Chem. Phys.*, 2011, **13**, 2809–2814.
- 49 C. H. Fang, H. L. Jia, S. Chang, Q. F. Ruan, P. Wang, T. Chen and J. F. Wang, *Energy Environ. Sci.*, 2014, **7**, 3431–3438.
- 50 B. Liu, Y. Jiang, Y. Wang, S. Shang, Y. Ni, N. Zhang, M. Cao and C. Hu, *Catal. Sci. Technol.*, 2018, **8**, 1094–1103.
- 51 Q. F. Ruan, L. Shao, Y. W. Shu, J. F. Wang and H. K. Wu, *Adv. Opt. Mater.*, 2014, **2**, 65–73.
- 52 Z. F. Bian, T. Tachikawa, P. Zhang, M. Fujitsuka and T. Majima, *J. Am. Chem. Soc.*, 2014, **136**, 458–465.

